Orbit-Transfer Torque Driven Field-Free Switching of Perpendicular Magnetization

Xing-Guo Ye(叶兴国)[†], Peng-Fei Zhu(朱鹏飞)[†], Wen-Zheng Xu(徐文正)[†], Nianze Shang(尚念泽),
Kaihui Liu(刘开辉), and Zhi-Min Liao(廖志敏)[*]

*State Key Laboratory for Mesoscopic Physics and Frontiers Science Center for Nano-optoelectronics,
School of Physics, Peking University, Beijing 100871, China*

The reversal of perpendicular magnetization (PM) by electric control is crucial for high-density integration of low-power magnetic random-access memory. Although the spin-transfer torque and spin-orbit torque technologies have been used to switch the magnetization of a free layer with perpendicular magnetic anisotropy, the former has limited endurance because of the high current density directly through the junction, while the latter requires an external magnetic field or unconventional configuration to break the symmetry. Here we propose and realize the orbit-transfer torque (OTT), that is, exerting torque on the magnetization using the orbital magnetic moments, and thus demonstrate a new strategy for current-driven PM reversal without external magnetic field. The perpendicular polarization of orbital magnetic moments is generated by a direct current in a few-layer WTe_2 due to the existence of nonzero Berry curvature dipole, and the polarization direction can be switched by changing the current polarity. Guided by this principle, we construct the WTe_2/Fe_3GeTe_2 heterostructures to achieve the OTT driven field-free deterministic switching of PM.

Magnetic random-access memory (MRAM)[1−4] as a type of non-volatile memory has advantages of high speed, low power consumption and high reliability, which is recently being developed by using magnetic tunnel junction (MTJ) with perpendicular magnetic anisotropy (PMA) for further scaling down.[5] The perpendicular magnetization (PM) reversal of the free layer is the key operation of data writing in MRAM.[6] The magnetization switch driven by spin-transfer torque effect[7−10] has been implemented in two-terminal MTJ, which challenges its durability due to the high-density current passing through the junction. Thereafter, three-terminal spin-orbit torque (SOT)[11−28] devices have been developed, where the magnetization switching is caused by interfacial spin accumulations coming from spin Hall effect,[13,14] Rashba effect,[12] or the topological surface states.[16] However, an external magnetic field is usually needed for the PM switching driven by SOT effect,[15] although a few experiments have demonstrated the SOT-induced filed-free PM switching by introducing interfacial exchange bias[22] or structure asymmetry,[17,25] which is unfavorable for realistic applications. In this Letter, we propose and demonstrate the orbit-transfer torque (OTT) effect to obtain the current-driven field-free PM switching. Instead of spin degree of freedom, the OTT effect exploits the polarization of orbital magnetic moment of Bloch electrons.[29]

Orbit-Transfer Torque as a New Strategy for PM Switching. The recently discovered Berry curvature dipole[30] in van der Waals materials offers an ideal platform to generate the perpendicularly polarized orbital magnetic moments by applying dc current,[31] formulated as $\boldsymbol{m} \propto (\boldsymbol{D} \cdot \boldsymbol{E})\hat{\boldsymbol{z}}$, where $\boldsymbol{D}$ is the Berry curvature dipole and $\boldsymbol{E}$ is the applied electric field. Similar to the SOT, OTT also has two components, i.e., field-like torque $T_{\mathrm{FL}} \sim \boldsymbol{M} \times \hat{\boldsymbol{m}}$, and antidamping-like torque $T_{\mathrm{AD}} \sim \boldsymbol{M} \times (\hat{\boldsymbol{m}} \times \boldsymbol{M})$ (Ref. [23]), where $\boldsymbol{M}$ is the magnetization of adjacent magnetic layer, and $\hat{\boldsymbol{m}}$ is the unit vector of polarized orbital magnetic moment. For perpendicularly polarized $\hat{\boldsymbol{m}}$, nonzero antidamping-like torque would emerge as long as $\boldsymbol{M}$ has a slight deviation from the perpendicular direction. For ferromagnetic materials with PMA, either spin wave excitation[32] or spin fluctuations can produce a perturbation of spin orientation deviating from the perpendicular direction. Therefore, the OTT can force the magnetization to prefer along the orbital polarization direction, as shown in Figs. 1(a) and 1(b).

A simplified analysis is carried out to search the candidate materials to generate OTT. First, we focus on the two-dimensional (2D) layered materials, where the dimension constraint forces the orbital magnetic moment along out-of-plane direction. Second, for 2D materials with nonzero Berry curvature dipole, such as

---

bilayer[33] or few-layer WTe$_2$ (Ref. [34]), and strained WSe$_2$ (Ref. [35]), current can induce the polarization of orbital magnetic moment.[31] As shown in Fig. 1(c), Berry curvature distributes asymmetrically in one single valley in these materials, forming a Berry curvature dipole. Applying a parallel dc current, the orbital magnetic moment is thus polarized. Further, as shown in Fig. 1(d), when the applied current polarity is reversed, the polarization direction of the orbital magnetic moment is also reversed.

Guided by this principle, we constructed the few-layer WTe$_2$/Fe$_3$GeTe$_2$ heterostructures (see Device Fabrication in the Supplemental Material), where the few-layer WTe$_2$ with nonzero Berry curvature dipole is used to generate the polarization of orbital magnetic moment by applying current, and the few-layer Fe$_3$GeTe$_2$ is used as the ferromagnetic layer with PMA.[36] Field-free current-driven magnetization switching has been demonstrated as a result of the OTT effect at the heterostructure interface. The measurement results of four devices, device A in the main text and devices B–D in Figs. S7–S9 and Table S1 in the Supplemental Material, are presented.
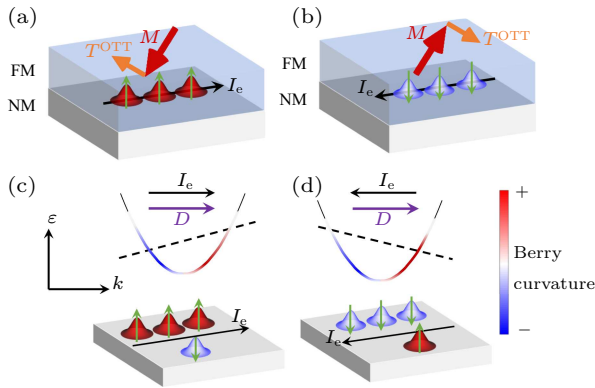

Fig. 1. Illustration of orbit-transfer torque. [(a), (b)] For the ferromagnetism (FM)/non-magnetic material (NM) heterostructure, the polarization of orbital magnetic moment can result in orbit-transfer torque that acts on the magnetization, and the up and down magnetization states can be switched by changing the current direction. [(c), (d)] Illustration of current-induced polarization of orbital magnetic moment in systems with nonzero Berry curvature dipole. The orbital magnetic moment is denoted by green arrow. Bloch electrons with opposite Berry curvature are denoted by red and blue, respectively. I_e is the electron current, D is the Berry curvature dipole, ε is the energy, and k is the wavevector.

Polarization of Orbital Magnetic Moment Manifested by Nonlinear Hall Effect. WTe$_2$ is a 2D layered van der Waals material belonging to the transition metal dichalcogenide family, with T$_d$-phase as its stable structure.[37] Monolayer T$_d$-WTe$_2$ consists of a layer of W atoms sandwiched between two layers of Te atoms in a distorted octahedral coordination, as shown in Fig. 2(a). WTe$_2$ possesses various exotic phases, including Weyl semimetal,[38] gate-tunable superconductivity,[39,40] quantum spin Hall

insulator,[41,42] and possible exciton insulator,[43] depending on its thickness. Its bulk crystal has space group $Pmn2_1$, which possesses a mirror symmetry along b axis mirror line [red line in Fig. 2(a)] and a glide mirror symmetry along a axis mirror line.[34] These two mirror symmetries recover an inversion symmetry in the ab plane, leading to vanishing Berry curvature dipole in the WTe$_2$ bulk. However, since the glide mirror symmetry involves a half-cell translation, it is generally broken at the surfaces, giving rise to nonzero Berry curvature dipole at surfaces.[44] Because the mirror symmetry with bc plane as mirror plane still exists at the surface, it constrains the Berry curvature dipole in WTe$_2$ along a axis direction. The nonzero Berry curvature dipole in few-layer WTe$_2$ has been observed in previous experiments,[34] evidenced by the nonlinear Hall effect.
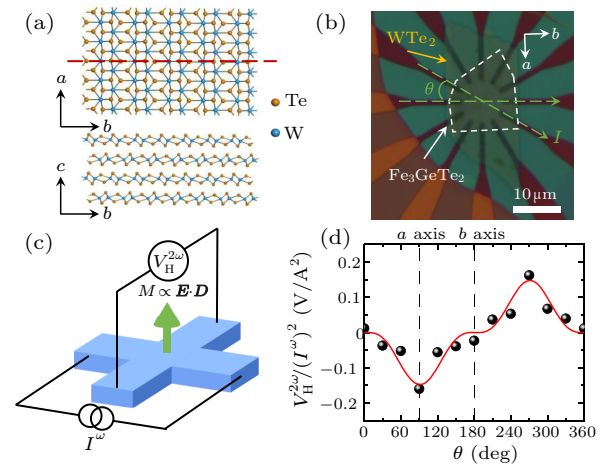

Fig. 2. Nonlinear Hall effect in WTe$_2$/Fe$_3$GeTe$_2$ heterostructures. (a) Crystal structure of T$_d$-WTe$_2$. The red line corresponds to the mirror line in the ab plane, which persists at the surface. (b) The optical image of device A, which consists of a WTe$_2$/Fe$_3$GeTe$_2$ heterostructure. The crystalline axes are aligned with electrodes. The θ is defined as the angle between the current direction and the baseline direction of the electrode pair, which is approximately along the b axis of WTe$_2$. For device A, the baseline direction is ~1.3° misaligned with b axis. (c) Schematic of the measurement configuration for nonlinear Hall effect. (d) The angle-dependence of the second-order nonlinear Hall effect at 1.8 K. The red line is the fitting curve.

The optical image of fabricated WTe$_2$/Fe$_3$GeTe$_2$ heterostructure, device A, is shown in Fig. 2(b). The thickness of WTe$_2$ and Fe$_3$GeTe$_2$ measured by an atomic force microscope is 11.9 and 11.2 nm, respectively (see Fig. S1). The multiple electrodes were designed as a circular disc configuration, which was utilized to implement the angle-dependent measurements. By identifying long, straight edges of WTe$_2$ and combining with polarized Raman spectroscopy, the crystalline axes were aligned with the electrodes, where the misalignment is ~1.3° for device A (see Fig. S2). The angle θ is defined in Fig. 2(b), where $\theta = 0°$ approximately corresponds to b axis; while $\theta =$

90° approximately corresponds to a axis. The device shows two carrier transport properties and large magnetoresistance with electron mobility $\sim$2203 cm^2/V·s (see Fig. S3). Since nonzero Berry curvature dipole emerges at the interface, when applying an electric field, it would give rise to the polarization of orbital magnetic moment, expressed as $\boldsymbol{m} \propto (\boldsymbol{D} \cdot \boldsymbol{E})\hat{\boldsymbol{z}}$ (Refs. [31,45]). When an ac current I^ω with frequency ω is applied, the induced orbital magnetization will have the alternating characteristic of frequency ω, further resulting in a second-harmonic anomalous Hall voltage $V_H^{2\omega}$ with frequency 2ω, known as the nonlinear Hall effect,[35] as illustrated in Fig. 2(c). The results are displayed in Fig. S4(a), and quadric $I^\omega - V_H^{2\omega}$ characteristics are observed. Moreover, the nonlinear Hall voltage shows the maximum at $\theta = 90°$ approximately along a axis and is nearly zero at $\theta = 0°$ approximately along b axis [see Fig. 2(d)]. This angle dependence is consistent with the fact that the Berry curvature dipole in few-layer WTe$_2$ is along the crystal a axis.

Orbit-Transfer Torque in WTe$_2$/Fe$_3$GeTe$_2$ Heterostructures. The hysteresis loops of Hall resistance (R_{xy}) of the WTe$_2$/Fe$_3$GeTe$_2$ heterostructure were measured by sweeping the out-of-plane magnetic field

at various temperatures. From the Arrott plots (see Fig. S5), it is found that the Curie temperature is $\sim$180 K, corresponding to that of 14-layer Fe$_3$GeTe$_2$ based on the previous work.[36] As shown in Fig. 3(a) and Fig. S6, the R_{xy} hysteresis loops with sharp transitions are clearly observed, consistent with the PMA characteristics of Fe$_3$GeTe$_2$ (Refs. [36,46]). To demonstrate the field-free switching of magnetization in the Fe$_3$GeTe$_2$ layer through OTT, a pulse-like dc current I_p was injected into the heterostructure at $\theta = 90°$ approximately along a axis, and the R_{xy} was measured after the pulse I_p was removed. As shown in Fig. 3(b), current-induced R_{xy} change is clearly observed at 130 K. The height of the R_{xy}–I_p loop agrees well with that of the R_{xy}–H loop in Fig. 3(a), indicating the deterministic PM switching. Therefore, the R_{xy}–I_p loops indicate that the upward and downward magnetization states in Fe$_3$GeTe$_2$ can be switched between each other by injecting opposite currents. Since no external magnetic field is applied, such PM switching is failed to be attributed to the SOT effect in WTe$_2$ (Ref. [27]). The current induced PM switching agrees well with the OTT effect, that is, the torque exerted by the perpendicularly polarized orbital magnetic moments.
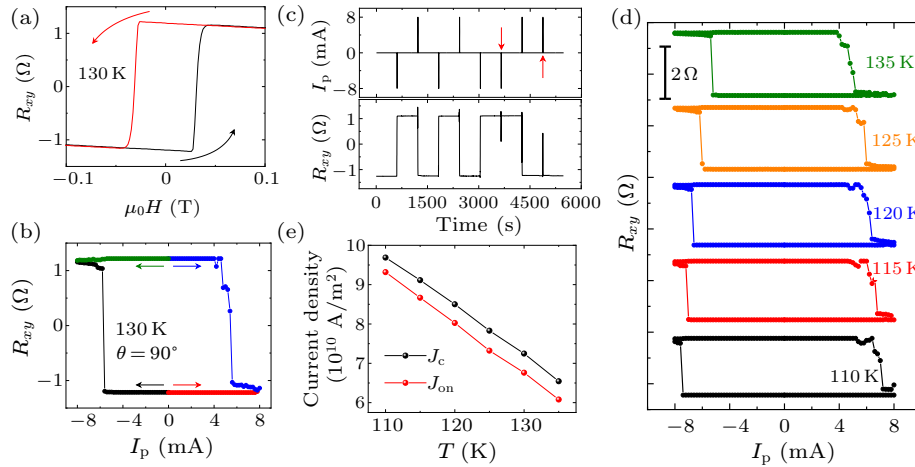

Fig. 3. Orbit-transfer torque induced field-free perpendicular magnetization switching in WTe$_2$/Fe$_3$GeTe$_2$ heterostructure. (a) Hall resistance as a function of magnetic field at 130 K. The hysteresis loop is used for reference to identify the magnetization states. (b) Hall resistance as a function of pulse current I_p at 130 K. Before sweeping I_p from zero to large positive or negative values, the magnetization state is initialized by magnetic field. (c) Upper: a series of current pulse with amplitude ± 8 mA is injected at 130 K. The red arrows indicate the deliberately programmed disturbing current pulses. Lower: the corresponding changes in Hall resistance. (d) Temperature dependence of the current-driven magnetization switching. The curves are shifted for clarity. (e) The temperature dependence of critical switching current density. The J_c corresponds to the current density at which resistance changes by more than half, and J_{on} corresponds to the current density at the onset of resistance change. The data in this figure were measured when the current was applied approximately along a axis at $\theta = 90°$.

A sequence of current pulse with amplitude ± 8 mA at 130 K and $\theta = 90°$ was injected into this heterostructure, as shown in Fig. 3(c). Current pulse with opposite polarity yields terminate states with saturated magnetization along opposite directions (up or down). Once the magnetization state is finalized, the disturbing current pulse will not affect the magnetization state, as indicated by the red arrows in Fig. 3(c).

Such robust magnetization switching against perturbations indicates the application potential in MRAM. Temperature dependence of this current-induced PM switching is further investigated, as shown in Fig. 3(d). Two critical switching current densities J_c and J_{on} are defined, where J_c corresponds to the current density at which resistance changes by more than half, and J_{on} corresponds to the current density at the onset of

resistance change. Both J_c and J_{on} are taken as the averages for up-to-down and down-to-up PM switching. As shown in Fig. 3(e), the J_c and J_{on} decrease upon increasing temperature, consistent with the fact that the effective PMA field in Fe_3GeTe_2 decreases upon increasing temperature.

Synergistic Effect of Spin-Orbit Torque and Orbit-Transfer Torque. The above results indicate the OTT-driven PM switching as the current was applied along a axis of WTe_2. It would be very different as the pulse current I_p is applied at $\theta = 0°$ approximately along b axis, where the current direction is perpendicular to the Berry curvature dipole and there is almost no current induced orbital magnetism. As shown in Fig. 4(a), no deterministic switching is observed when I_p is along b axis at 130 K. Instead of switching between upward and downward PM states, I_p along b axis yields a terminate state with nearly zero Hall resistance. This is well understood by the SOT-induced multi-domain scenario.[28] Since SOT forces the magnetization lying in plane, when removing pulse current and thus SOT, multi-domains with magnetization randomly upward or downward would emerge, leading to nearly zero Hall resistance. Thus, the OTT is absent, and SOT dominates when I_p is along b axis, as expected.

Using the disc distributed electrode structure of the device, angle dependence of current-driven magnetization switching was investigated at 130 K, as shown in Fig. 4(b). It is found that the deterministic switching can be obtained within a large angle window due to the nonzero current component along a axis, as shown by the R_{xy}–I_p loops at $\theta = 120°$ and $60°$ in Fig. 4(b). As for the current along direction closer to b axis, that is, $\theta = 30°$ and $150°$, the R_{xy}–I_p loops only shows partially switching without reaching the saturated magnetization states, which suggests the coexistence of SOT and OTT. The angle-dependent critical switching current density is shown in Fig. 4(c). The J_c is failed to be fitted in the form of $1/\cos(\theta - 90°)$ when only considering the current component parallel to a axis. Because the bulk states can also contribute to the SOT due to intrinsic spin-orbit coupling and the OTT only comes from the interface due to the need of symmetry breaking, the strength of SOT should be larger than that of OTT in the WTe_2/Fe_3GeTe_2 device. Therefore, the SOT may dominate the onset change of magnetic states, but the deterministic switching is achieved through OTT. The angle dependence of the onset switching current density J_{on} is consistent with the anisotropy of spin-orbit coupling in bulk WTe_2, which possesses the largest strength along b axis.[27] It is worth noting that the critical switching current at $\theta = 60°$ and $120°$ shows a smaller value than that at $\theta = 90°$, suggesting that the synergy of SOT and OTT is more effective for the PM switching.

It is worth noting that some works point out that

out-of-plane spin accumulation may occur together with SOT in WTe_2 (Ref. [47]). Although this out-of-plane spin accumulation is a possible origination of the field-free perpendicular magnetization switching, it can be ruled out in our work due to the following two reasons. First, our results demonstrate the anisotropic angle dependence of the magnetization switching, which is not expected for the mechanism of out-of-plane spin accumulation. In contrast, this angle dependence is naturally explained by OTT. Second, the SOT in WTe_2 was reported to be mainly contributed by bulk states,[27] however, our results show that the switching critical current density is almost the same in samples with different thicknesses (see Table S1), indicating a surface origin of the antidamping torque. This surface origin is also well consistent with the mechanism of OTT.
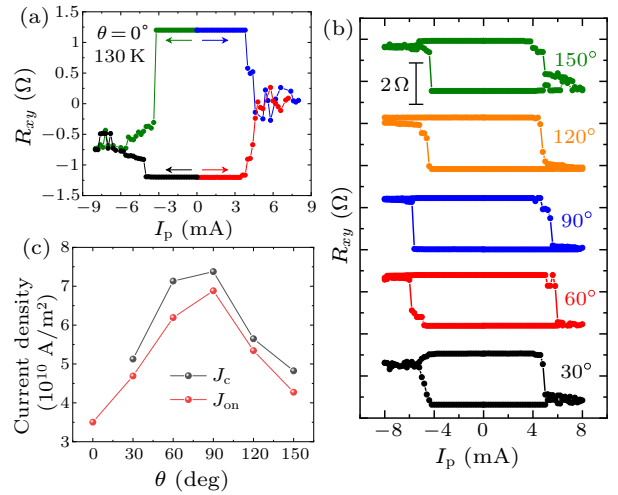

Fig. 4. Angle-dependence of current-driven magnetization switching in WTe_2/Fe_3GeTe_2 heterostructure. (a) Hall resistance as a function of pulse current I_p at 130 K. I_p is applied at $\theta = 0°$ approximately along b axis. Before sweeping I_p from zero to large positive or negative values, the magnetization state is initialized by magnetic field. (b) The R_{xy}–I_p loops at 130 K with I_p applied along different angle θ. The curves are shifted for clarity. (c) The critical switching current density as a function of angle θ.

Outlook. Our work demonstrates the OTT as a new strategy for field-free magnetization switching in PMA ferromagnets, which utilizes the orbital magnetic moment of Bloch electrons rather than spins, thus extending the concept from spintronics to orbitronics and their hybrid. Through symmetry analysis, we propose that besides few-layer WTe_2, 2D materials with nonzero Berry curvature dipole,[48] including bilayer WTe_2 (Ref. [33]), strained WSe_2 (Ref. [35]), few-layer $MoTe_2$ (Ref. [49]), and corrugated bilayer graphene,[50] are candidates to realize OTT. Moreover, the temperature dependence of current-driven switching indicates that OTT is robust against temperature. By building heterostructures using PMA materials with Curie temperature above 300 K, such as few-layer $CrTe_2$ (Ref. [51]), room-temperature PM

switching through OTT can be achieved, promising for realistic applications.

References

[1] Ohno H, Chiba D, Matsukura F, Omiya T, Abe E, Dietl T, Ohno Y and Ohtani K 2000 *Nature* **408** 944
[2] Myers E B, Ralph D C, Katine J A, Louie R N and Buhrman R A 1999 *Science* **285** 867
[3] Wegrowe J E, Kelly D, Jaccard Y, Guittienne Ph and Ansermet J Ph 1999 *Europhys. Lett.* **45** 626
[4] Chappert C, Fert A and van dau Frédéric N 2007 *Nat. Mater.* **6** 813
[5] Moser A, Takano K, Margulies D T, Albrecht M, Sonobe Y, Ikeda Y, Sun S and Fullerton E E 2002 *J. Phys. D* **35** R157
[6] Miron I M, Garello K, Gaudin G, Zermatten P J, Costache M V, Auffret S, Bandiera S, Rodmacq B, Schuhl A and Gambardella P 2011 *Nature* **476** 189
[7] Berger L 1996 *Phys. Rev. B* **54** 9353
[8] Slonczewski J C 1996 *J. Magn. Magn. Mater.* **159** L1
[9] Ralph D C and Stiles M D 2008 *J. Magn. Magn. Mater.* **320** 1190
[10] Pai C F, Liu L, Li Y, Tseng H W, Ralph D C and Buhrman R A 2012 *Appl. Phys. Lett.* **101** 122404
[11] Chernyshov A, Overby M, Liu X, Furdyna J K, Lyanda-Geller Y and Rokhinson L P 2009 *Nat. Phys.* **5** 656
[12] Miron I M, Gaudin G, Auffret S, Rodmacq B, Schuhl A, Pizzini S, Vogel J and Gambardella P 2010 *Nat. Mater.* **9** 230
[13] Liu L, Pai C F, Li Y, Tseng H W, Ralph D C and Buhrman R A 2012 *Science* **336** 555
[14] Liu L, Lee O J, Gudmundsen T J, Ralph D C and Buhrman R A 2012 *Phys. Rev. Lett.* **109** 096602
[15] Garello K, Miron I M, Avci C O, Freimuth F, Mokrousov Y, Blügel S, Auffret S, Boulle O, Gaudin G and Gambardella P 2013 *Nat. Nanotechnol.* **8** 587
[16] Mellnik A R, Lee J S, Richardella A, Grab J L, Mintun P J, Fischer M H, Vaezi A, Manchon A, Kim E A, Samarth N and Ralph D C 2014 *Nature* **511** 449
[17] Yu G, Upadhyaya P, Fan Y, Alzate J G, Jiang W, Wong K L, Takei S, Bender S A, Chang L T, Jiang Y, Lang M, Tang J, Wang Y, Tserkovnyak Y, Amiri P K and Wang K L 2014 *Nat. Nanotechnol.* **9** 548
[18] Fan Y, Upadhyaya P, Kou X, Lang M, Takei S, Wang Z, Tang J, He L, Chang L T, Montazeri M, Yu G, Jiang W, Nie T, Schwartz R N, Tserkovnyak Y and Wang K L 2014 *Nat. Mater.* **13** 699
[19] Kurebayashi H, Sinova J, Fang D, Irvine A C, Skinner T D, Wunderlich J, Novák V, Campion R P, Gallagher B L, Vehstedt E K, Zârbo L P, Výborný K, Ferguson A J and Jungwirth T 2014 *Nat. Nanotechnol.* **9** 211
[20] Fukami S, Anekawa T, Zhang C and Ohno H 2016 *Nat. Nanotechnol.* **11** 621
[21] Wadley P, Howells B, Železny J *et al.* 2016 *Science* **351** 587
[22] Fukami S, Zhang C, DuttaGupta S, Kurenkov A and Ohno H 2016 *Nat. Mater.* **15** 535
[23] Manchon A, Železný J, Miron I M, Jungwirth T, Sinova J, Thiaville A, Garello K and Gambardella P 2019 *Rev. Mod. Phys.* **91** 035004
[24] MacNeill D, Stiehl G M, Guimaraes M H D, Buhrman R A, Park J and Ralph D C 2017 *Nat. Phys.* **13** 300
[25] Cai K, Yang M, Ju H, Wang S, Ji Y, Li B, Edmonds K W, Sheng Y, Zhang B, Zhang N, Liu S, Zheng H and Wang K 2017 *Nat. Mater.* **16** 712
[26] Baek S C, Amin V P, Oh Y W, Go G, Lee S J, Lee G H, Kim K J, Stiles M D, Park B G and Lee K J 2018 *Nat. Mater.* **17** 509
[27] Shi S, Liang S, Zhu Z, Cai K, Pollard S D, Wang Y, Wang J, Wang Q, He P, Yu J, Eda G, Liang G and Yang H 2019 *Nat. Nanotechnol.* **14** 945
[28] Wang X, Tang J, Xia X, He C, Zhang J, Liu Y, Wan C, Fang C, Guo C, Yang W, Guang Y, Zhang X, Xu H, Wei J, Liao M, Lu X, Feng J, Li X, Peng Y, Wei H, Yang R, Shi D, Zhang X, Han Z, Zhang Z, Zhang G, Yu G and Han X 2019 *Sci. Adv.* **5** eaaw8904
[29] Chang M C and Niu Q 1996 *Phys. Rev. B* **53** 7010
[30] Sodemann I and Fu L 2015 *Phys. Rev. Lett.* **115** 216806
[31] Lee J, Wang Z, Xie H, Mak K F and Shan J 2017 *Nat. Mater.* **16** 887
[32] Corciovei A 1963 *Phys. Rev.* **130** 2223
[33] Ma Q, Xu S Y, Shen H, MacNeill D, Fatemi V, Chang T R, Valdivia A M M, Wu S, Du Z, Hsu C H, Fang S, Gibson Q D, Watanabe K, Taniguchi T, Cava R J, Kaxiras E, Lu H Z, Lin H, Fu L, Gedik N and Jarillo-Herrero P 2019 *Nature* **565** 337
[34] Kang K, Li T, Sohn E, Shan J and Mak K F 2019 *Nat. Mater.* **18** 324
[35] Qin M S, Zhu P F, Ye X G, Xu W Z, Song Z H, Liang J, Liu K and Liao Z M 2021 *Chin. Phys. Lett.* **38** 017301
[36] Deng Y, Yu Y, Song Y, Zhang J, Wang N Z, Sun Z, Yi Y, Wu Y Z, Wu S, Zhu J, Wang J, Chen X H and Zhang Y 2018 *Nature* **563** 94
[37] Brown B E 1966 *Acta Crystallogr.* **20** 268
[38] Ali M N, Xiong J, Flynn S, Tao J, Gibson Q D, Schoop L M, Liang T, Haldolaarachchige N, Hirschberger M, Ong N P and Cava R J 2014 *Nature* **514** 205
[39] Fatemi V, Wu S, Cao Y, Bretheau L, Gibson Q D, Watanabe K, Taniguchi T, Cava R J and Jarillo-Herrero P 2018 *Science* **362** 926
[40] Sajadi E, Palomaki T, Fei Z, Zhao W, Bement P, Olsen C, Luescher S, Xu X, Folk J A and Cobden D H 2018 *Science* **362** 922
[41] Tang S, Zhang C, Wong D, Pedramrazi Z, Tsai H Z, Jia C, Moritz B, Claassen M, Ryu H, Kahn S, Jiang J, Yan H, Hashimoto M, Lu D, Moore R G, Hwang C C, Hwang C, Hussain Z, Chen Y, Ugeda M M, Liu Z, Xie X, Devereaux T P, Crommie M F, Mo S K and Shen Z X 2017 *Nat. Phys.* **13** 683
[42] Wu S, Fatemi V, Gibson Q D, Watanabe K, Taniguchi T, Cava R J and Jarillo-Herrero P 2018 *Science* **359** 76
[43] Wang P, Yu G, Jia Y, Onyszczak M, Cevallos F A, Lei S, Klemenz S, Watanabe K, Taniguchi T, Cava R J, Schoop L M and Wu S 2021 *Nature* **589** 225
[44] You J S, Fang S, Xu S Y, Kaxiras E and Low T 2018 *Phys. Rev. B* **98** 121109
[45] Son J, Kim K H, Ahn Y H, Lee H W and Lee J 2019 *Phys. Rev. Lett.* **123** 036806
[46] Shao Y, Lv W, Guo J, Qi B, Lv W, Li S, Guo G and Zeng Z 2020 *Appl. Phys. Lett.* **116** 092401
[47] Zhao B, Karpiak B, Khokhriakov D, Johansson A, Hoque A M, Xu X, Jiang Y, Mertig I and Dash S P 2020 *Adv. Mater.* **32** 2000818
[48] Du Z Z, Lu H Z and Xie X C 2021 *Nat. Rev. Phys.* **3** 744
[49] Zhang Y, van den Brink J, Felser C and Yan B 2018 *2D Mater.* **5** 044001
[50] Ho S C, Chang C H, Hsieh Y C, Lo S T, Huang B, Vu T H Y, Ortix C and Chen T M 2021 *Nat. Electron.* **4** 116
[51] Zhang X, Lu Q, Liu W, Niu W, Sun J, Cook J, Vaninger M, Miceli P F, Singh D J, Lian S W, Chang T R, He X, Du J, He L, Zhang R, Bian G and Xu Y 2021 *Nat. Commun.* **12** 2492

Supplemental Material for "Orbit-Transfer Torque Driven Field-Free Switching of Perpendicular Magnetization"

Xing-Guo Ye (叶兴国)[†], Peng-Fei Zhu（朱鹏飞）[†], Wen-Zheng Xu(徐文正)[†], Nianze Shang(尚念泽), Kaihui Liu(刘开辉), and Zhi-Min Liao(廖志敏)*

State Key Laboratory for Mesoscopic Physics and Frontiers Science Center for Nano-optoelectronics, School of Physics, Peking University; Beijing 100871, China.

*Corresponding author. Email: liaozm@pku.edu.cn

†These authors contributed equally to this work.

Device Fabrication

Few layer WTe_2 was obtained from high-quality artificially grown crystals of bulk WTe_2 commercially purchased from HQ Graphene through standard mechanically exfoliated method. Few layer Fe_3GeTe_2 was obtained in a similar way. Then we patterned Ti/Au electrodes (~10 nm thick) onto an individual SiO_2/Si substrate with a circular disc configuration through e-beam lithography, metal deposition and lift-off. To achieve a better contact, the electrodes were precleaned by air plasma. Exfoliated BN flake (~20 nm thick), few layer Fe_3GeTe_2 (~10-15 nm thick) and few layer WTe_2 (~2-15 nm thick) were sequentially picked up and then transferred onto the Ti/Au electrodes using a polymer-based dry transfer technique[1]. The whole exfoliated and transfer processes were done in an argon-filled glove box with O_2 and H_2O content below 0.01 parts per million to avoid sample degradation.

Polarized Raman spectroscopy of few-layer WTe_2

The Raman spectroscopy was measured with 514 nm excitation wavelengths through a linearly polarized solid-state laser beam. The polarization of the excitation laser was controlled by a half-wave plate and a polarizer. The Raman scattered light with the same polarization as the excitation laser were collected. As shown in Fig. S2b, five Raman peaks are observed, which belong to the A1 modes of WTe_2 (Ref. [2]). The polarization dependence of intensities of peaks P2 and P11 (denoted in Fig. S2b) are presented in Figs. S2c and S2d, respectively. Based on previous reports[2], the polarization direction with maximum intensity was assigned as the *b* axis. The determined crystalline axes, i.e., *a* axis and *b* axis, are further denoted by the black arrows in the optical image (Fig. S2a).

Transport Measurements

All transport measurements were carried out in an Oxford cryostat with a variable temperature insert and a superconducting magnet. First-, second- and third-harmonic voltage signals were collected by standard lock-in techniques (Stanford Research Systems Model SR830) with frequency ω = 17.777 Hz unless otherwise stated. A sequence of pulse-like d.c. current I_P was applied through a Keithley 2400 SourceMeter. I_P was swept in steps of 0.2 mA. After every I_P was applied and then removed, the Hall resistance was measured as applying a 0.1 mA bias a.c. current.

Basic Transport Properties of Device A

The resistivity ρ_{xx} of device A along *a* axis as a function of temperature was measured, as shown in Fig. S3a. By considering a parallel resistance model, we could obtain the resistivity of

WTe$_2$ by $\rho_{xx}^{WTe_2} = t_{WTe_2}\Big/(\frac{t}{\rho_{xx}} - \frac{t_{FGT}}{\rho_{xx}^{FGT}})$, where $\rho_{xx}^{WTe_2}$ is the resistivity of WTe$_2$, ρ_{xx}^{FGT} is the resistivity of Fe$_3$GeTe$_2$, t_{WTe_2} is the thickness of WTe$_2$, t_{FGT} is the thickness of Fe$_3$GeTe$_2$ and $t = t_{WTe_2} + t_{FGT}$. Referring to the $\rho_{xx}^{FGT}(T)$ previously reported by Z. Fei et al (Ref. [54]), the $\rho_{xx}^{WTe_2}$ was calculated and presented in Fig. S3a. Furthermore, the fraction of current flowing in the WTe$_2$ layer is estimated by $\frac{I_{WTe_2}}{I} = \frac{1}{1+\frac{\rho_{xx}^{WTe_2}}{\rho_{xx}^{FGT}}\frac{t_{FGT}}{t_{WTe_2}}}$, where I is the applied current flowing in the whole heterostructure, and I_{WTe_2} is the current component flowing in the WTe$_2$ layer. For other angles, $\rho_{xx}^{WTe_2}$ was estimated through the intrinsic resistivity anisotropy of WTe$_2$ following $\rho_{xx}(\theta) = \rho_a sin^2(\theta - \theta_0) + \rho_b cos^2(\theta - \theta_0)$, where ρ_a and ρ_b are resistivity along a axis and b axis, respectively, θ_0 corresponds to b axis.

The magneto-transport properties of device A at 1.8 K are shown in Fig. S3b. The large non-saturated magnetoresistance and Hall resistance demonstrate two-carrier transport characteristics, indicating a nearly compensated electron and hole density in WTe$_2$. Through a semi-classical two-carrier model[4], that is, $\rho_{xx} = \frac{1}{e}\frac{n\mu_n + p\mu_p + (n\mu_p + p\mu_n)\mu_n\mu_p B^2}{(n\mu_n + p\mu_p)^2 + (n-p)^2\mu_n^2\mu_p^2 B^2}$ and $\rho_{xy} = \frac{1}{e}\frac{(p\mu_p^2 - n\mu_n^2)B + (p-n)\mu_n^2\mu_p^2 B^3}{(n\mu_n + p\mu_p)^2 + (n-p)^2\mu_n^2\mu_p^2 B^2}$, where n is the electron density, p is the hole density, μ_n is the electron mobility and μ_p is the hole mobility, the carrier density and mobility are estimated as, $n = 1.51 \times 10^{13}\ cm^{-2}$, $p = 0.99 \times 10^{13}\ cm^{-2}$, $\mu_n = 2203\ cm^2/V \cdot s$ and $\mu_p = 1497\ cm^2/V \cdot s$.

Higher-order Hall effect in WTe$_2$

Due to the nonzero Berry curvature dipole on the surface, second-order nonlinear Hall effect is expected in few-layer WTe$_2$ (Ref.[34]). By utilizing the disc geometry of the electrodes, angle-dependence of the second-order nonlinear Hall effect was investigated, as shown in Fig. 2, which could help to confirm the alignment between electrodes and crystalline axis of WTe$_2$. Based on the symmetry of WTe$_2$, the second-order nonlinear Hall effect shows angle-dependence following $\frac{V_H^{2\omega}}{(I^\omega)^2} \propto sin(\theta - \theta_0)[d_{12}r^2 sin^2(\theta - \theta_0) + (d_{11} - 2d_{26}r^2)cos^2(\theta - \theta_0)]$ (Ref.[30]), where $V_H^{2\omega}$ is the second-harmonic Hall voltage, I^ω is the applied a.c. current, r is the resistance anisotropy, d$_{ij}$ are the elements of the second-order nonlinear susceptibility tensor for the Pm point group, θ_0 is the angle misalignment between $\theta = 0°$ and crystalline b axis. The fitting curve for this angle dependence is shown by the red line in Fig. 2d, which yields the misalignment θ_0 equals 1.3° in device A.

In addition to the second-order nonlinear Hall effect, it is recently also reported a third-order nonlinear Hall effect in the bulk of WTe$_2$ induced by the Berry connection polarizability tensor[5]. Fig. S4 shows the third-order nonlinear Hall effect in device A at 1.8 K. The third-order nonlinear Hall effect shows angle-dependence following $\frac{V_H^{3\omega}}{(I^\omega)^3} \propto cos(\theta - \theta_0)sin(\theta - \theta_0)[(\chi_{22}r^4 - 3\chi_{12}r^2)sin^2(\theta - \theta_0) + (3\chi_{21}r^2 - \chi_{11})cos^2(\theta - \theta_0)]$ (Ref.[47]), where $V_H^{3\omega}$ is the third-harmonic Hall voltage, χ_{ij} are elements of the third-order susceptibility tensor. The fitting curve for this angle dependence is shown by the red line in Fig. S4c, which yields a similar misalignment angle $\theta_0 \sim 1.3°$.
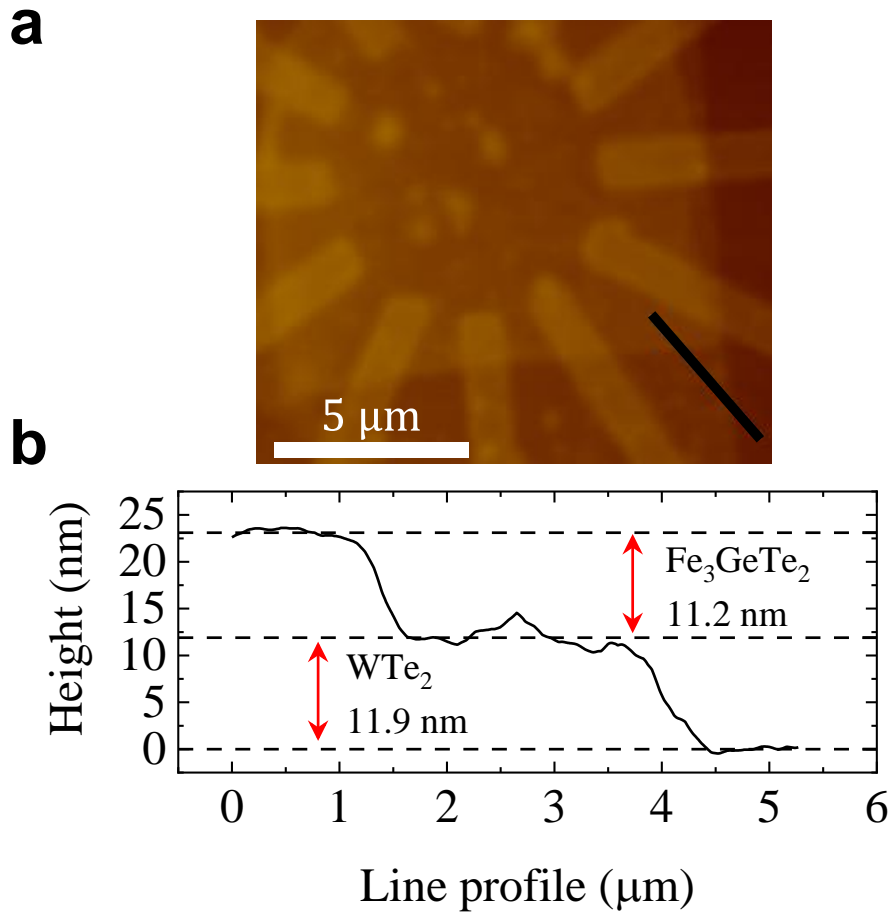
a

5 µm

b

Fe$_3$GeTe$_2$
11.2 nm

WTe$_2$
11.9 nm

Height (nm)

Line profile (µm)

Fig. S1 │ The atomic force microscope image of device A. The line profile shows the thickness of the WTe$_2$ is 11.9 nm, corresponding to 17-layer thickness. The thickness of the Fe$_3$GeTe$_2$ is 11.2 nm, corresponding to 14-layer thickness.
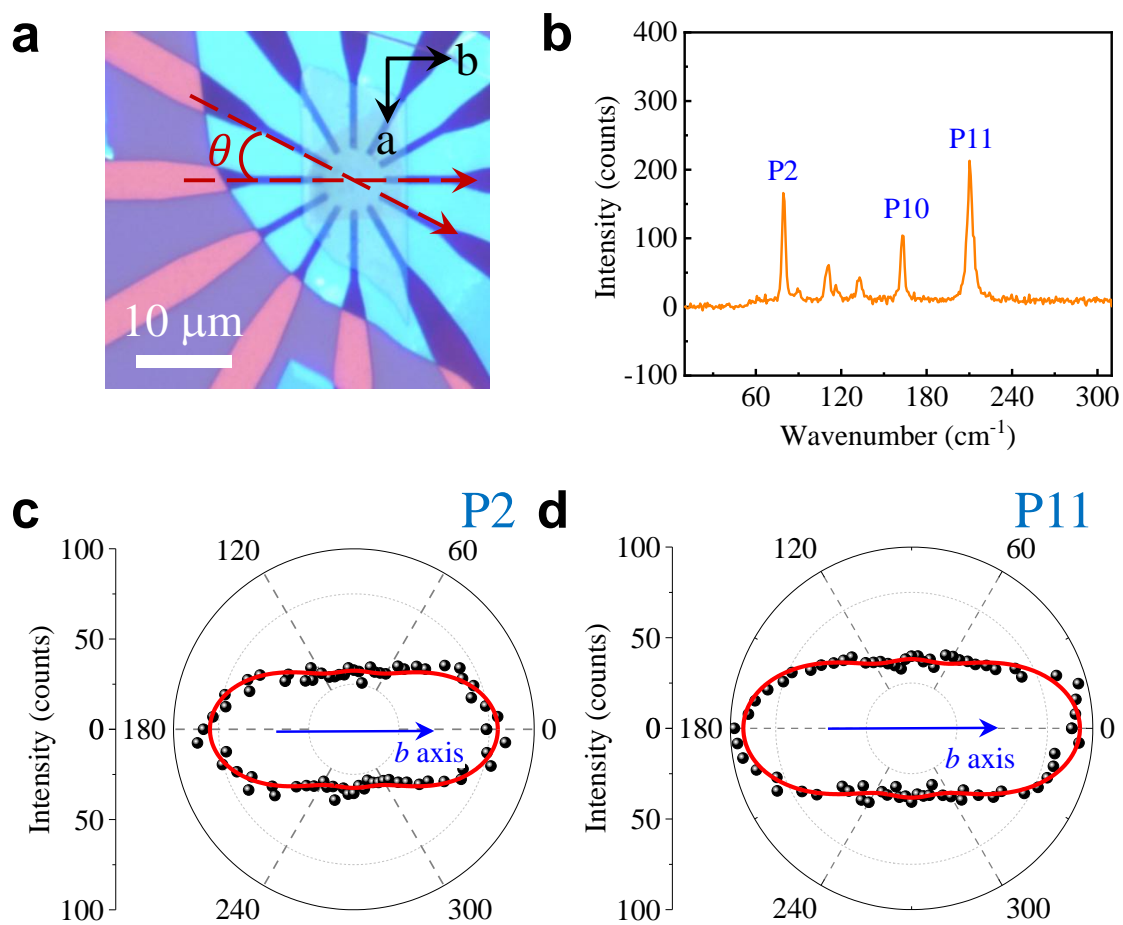
Fig. S2│Polarized Raman spectroscopy of few-layer WTe₂ to determine the crystalline orientation. a, The optical image of device A. **b,** A typical Raman spectrum of device A, where the polarization direction is approximately along *b* axis. **c,d,** Polarization dependence of intensities of peaks (**c**) P2 and (**d**) P11 for device A.
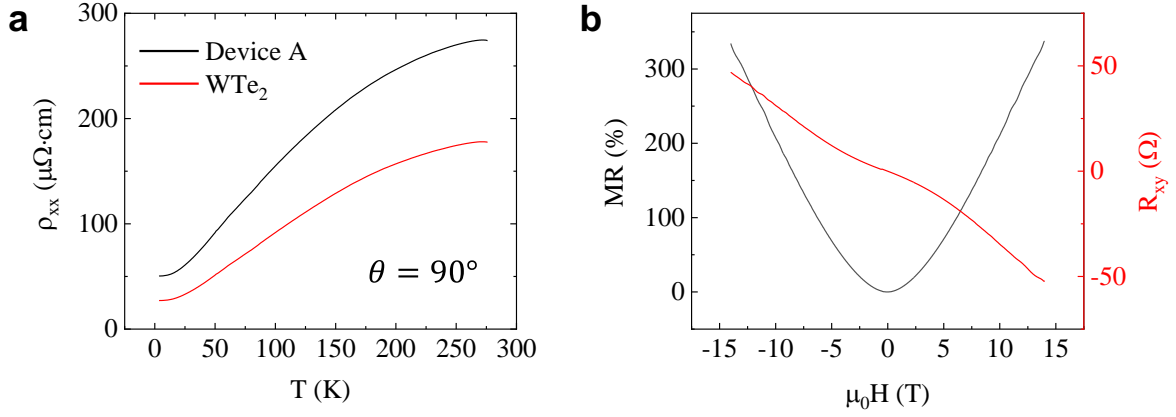
Fig. S3 │ Basic transport properties of device A. a, The resistivity as a function of temperature.
b, Magnetoresistance (MR) and Hall resistance as a function of magnetic field at 1.8 K, marked
by black and red, respectively. The MR is defined as $\frac{R_{xx}(\mu_0 H) - R_{xx}(0)}{R_{xx}(0)} \times 100\%$. The large non-
saturated MR and Hall resistance demonstrate two-carrier transport characteristics, indicating a
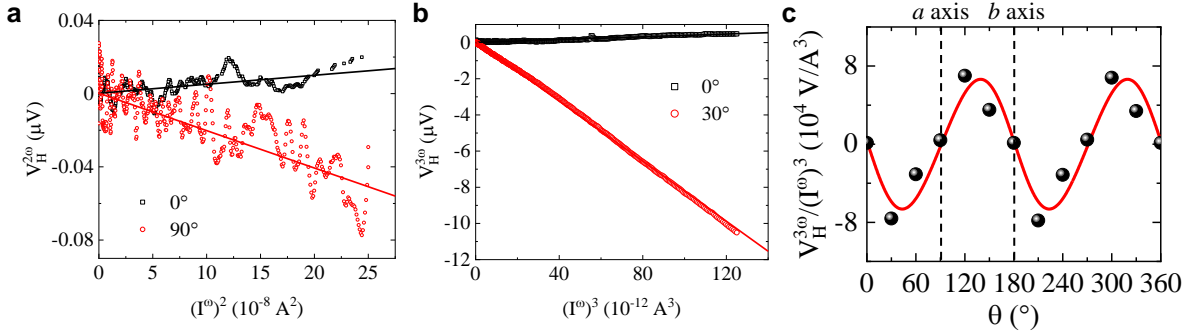nearly compensated electron and hole density in WTe$_2$.

Fig. S4 │ Higher-order nonlinear Hall effect in device A at 1.8 K. a, The second-order
nonlinear Hall voltage as a function of $(I^\omega)^2$, where I^ω along $\theta = 0°$ and $90°$ is marked by black
and red, respectively. **b,** The third-order nonlinear Hall voltage as a function of $(I^\omega)^3$, where I^ω
along $\theta = 0°$ and $30°$ is marked by black and red, respectively. **c,** The angle dependence of the
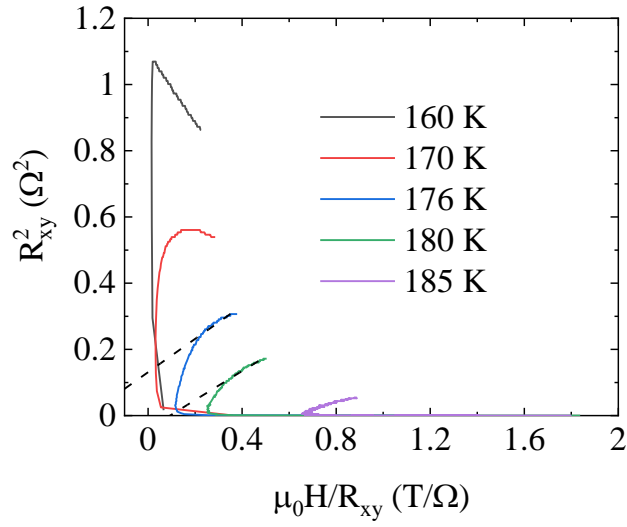third-order nonlinear Hall effect.

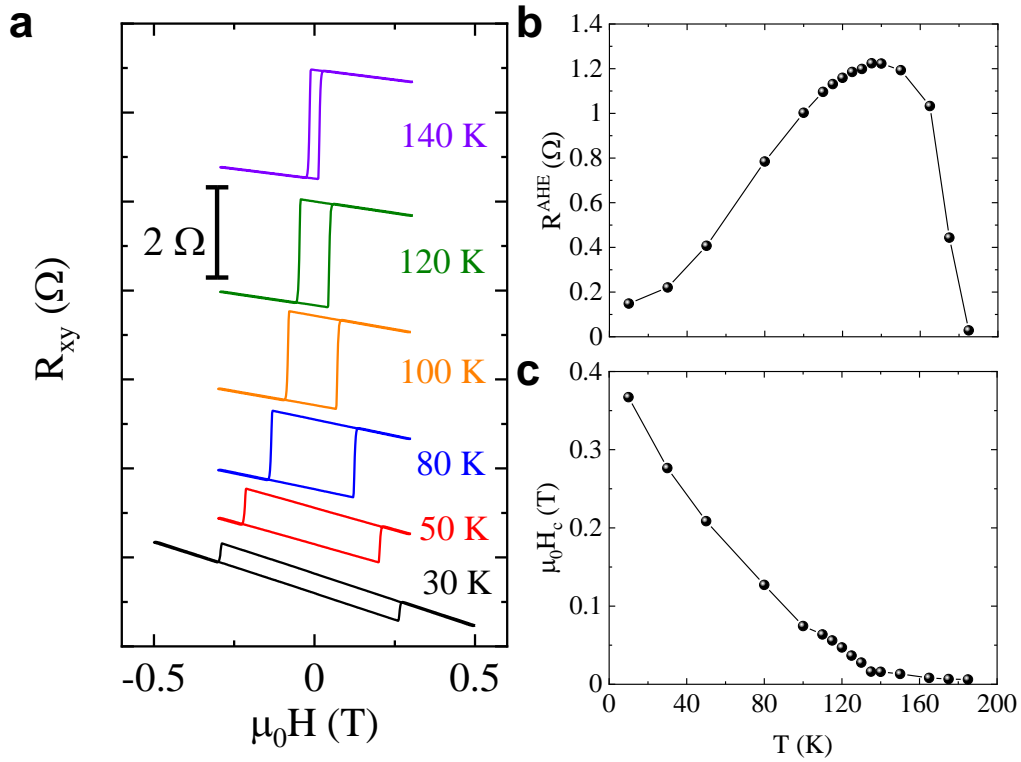**Fig. S5 │ Arrott plot of device A.** The Curie temperature ~180 K is estimated.

Fig. S6 │ Magnetic properties of device A. a, The Hall resistance as a function of magnetic field at various temperatures. **b,** The anomalous Hall resistance, defined as the half of the R-H loop height, as a function of temperature. **c,** The coercive field as a function of temperature.
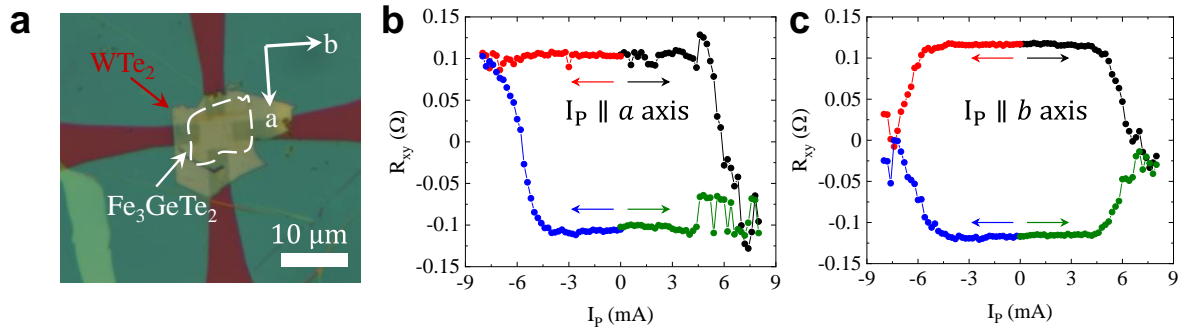
Fig. S7│Reproducible results in device B. a, The optical image of device B. **b, c,** Hall resistance as a function of pulse current I_P at 120 K for I_P approximately along a axis and b axis, respectively. Before sweeping I_P from zero to large positive or negative values, the magnetization state is initialized by perpendicular magnetic field.
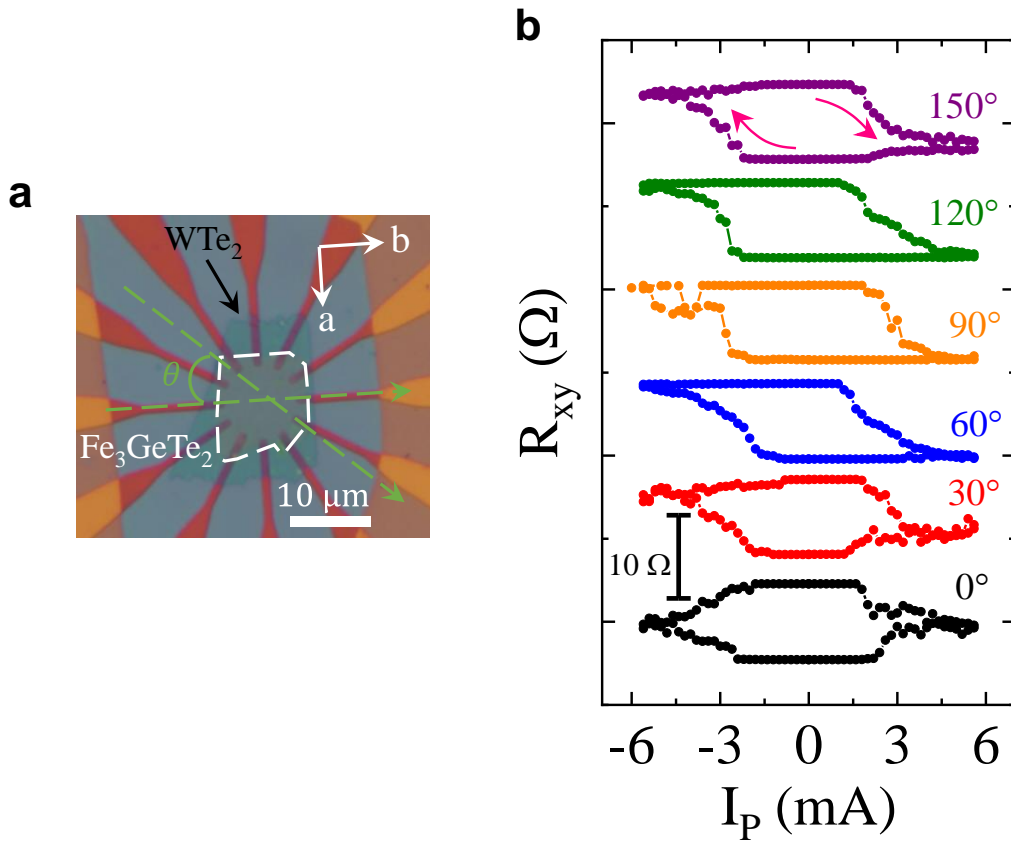

Fig. S8│Reproducible results in device C. a, The optical image of device C. **b,** The R_{xy}-I_P loops at 120 K with I_P applied along different angle θ. Before sweeping I_P from zero to large positive or negative values, the magnetization state is initialized by perpendicular magnetic field. The curves are shifted for clarity.
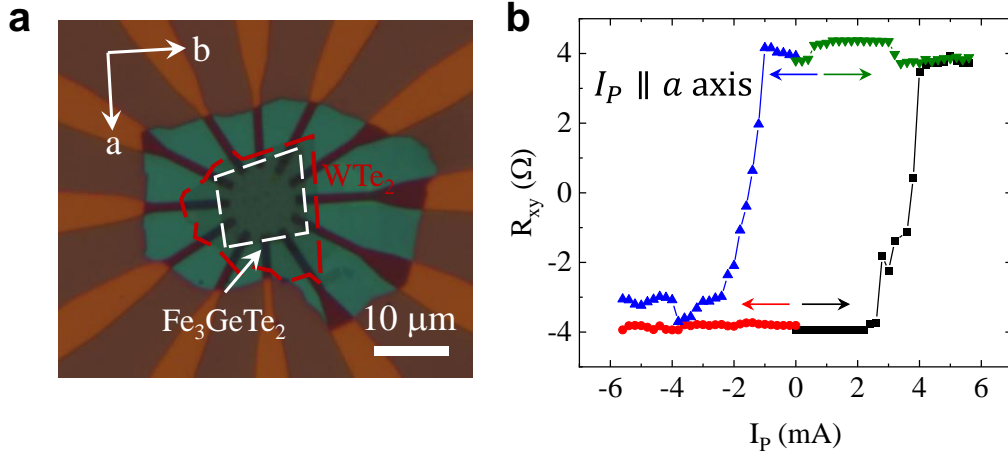
Fig. S9 │ Reproducible results in device D. a, The optical image of device D. **b,** Hall resistance as a function of pulse current I_P at 120 K. I_P is applied approximately along *a* axis. Before sweeping I_P from zero to large positive or negative values, the magnetization state is initialized by applying perpendicular magnetic field.

Table S1| Summary of the thickness of WTe$_2$ (t_{WTe_2}) and Fe$_3$GeTe$_2$ (t_{FGT}), and the switching current density J_c at 120 K along *a* axis in different devices.

Device	t_{WTe_2} *(nm)*	t_{FGT} *(nm)*	J_c (10^{10} A/m^2)
A	11.9	11.2	8.5
B	14.7	12	8.6
C	5.6	14.4	6.5
D	3.5	12	8.4

References

[1] Wang L, Meric I, Huang P Y, Gao Q, Gao Y, Tran H, Taniguchi T, Watanabe K, Campos L M, Muller D A, Guo J, Kim P, Hone J, Shepard K L and Dean C R. One-Dimensional Electrical Contact to a Two-Dimensional Material. *Science* **342** 614-617 (2013).

[2] Kim M, Han S, Kim J H, Lee J U, Lee Z and Cheong H. Determination of the thickness and orientation of few-layer tungsten ditelluride using polarized Raman spectroscopy. *2D Mater.* **3** 034004 (2016).

[3] Fei Z, Huang B, Malinowski P, Wang W, Song T, Sanchez J, Yao W, Xiao D, Zhu X, May A F, Wu W, Cobden D H, Chu J H and Xu X. Two-dimensional itinerant ferromagnetism in atomically thin Fe$_3$GeTe$_2$. *Nature Mater.* **17** 778–782 (2018).

[4] Fatemi V, Gibson Q D, Watanabe K, Taniguchi T, Cava R J and Jarillo-Herrero P Magnetoresistance and quantum oscillations of an electrostatically tuned semimetal-to-metal transition in ultrathin WTe$_2$. *Phys. Rev. B* **95** 041410 (2017).

[5] Lai S, Liu H, Zhang Z, Zhao J, Feng X, Wang N, Tang C, Liu Y, Novoselov K S, Yang S A and Gao W B. Third-order nonlinear Hall effect induced by the Berry-connection polarizability tensor. *Nat. Nanotechnol.* **16** 869–873 (2021).